

**A DETAILED STUDY OF NON-THERMAL X-RAY  
PROPERTIES AND INTERSTELLAR GAS TOWARD THE  
 $\gamma$ -RAY SUPERNOVA REMNANT RX J1713.7–3946**

H. Sano<sup>1</sup>, T. Fukuda<sup>1</sup>, S. Yoshiike<sup>1</sup>, J. Sato<sup>1</sup>, H. Horachi<sup>1</sup>, T. Kuwahara<sup>1</sup>, K. Torii<sup>1</sup>, T. Hayakawa<sup>1</sup>, T. Tanaka<sup>2</sup>, H. Matsumoto<sup>1</sup>, T. Inoue<sup>3</sup>, R. Yamazaki<sup>3</sup>, S. Inutsuka<sup>1</sup>, A. Kawamura<sup>4</sup>, H. Yamamoto<sup>1</sup>, T. Okuda<sup>4</sup>, K. Tachihara<sup>1</sup>, N. Mizuno<sup>4</sup>, T. Onishi<sup>5</sup>, A. Mizuno<sup>6</sup>, F. Acero<sup>7</sup>, and Y. Fukui<sup>1</sup>

<sup>1</sup>Department of Physics, Nagoya University, Furo-cho, Chikusa-ku, Nagoya 464-8601, Japan; sano@a.phys.nagoya-u.ac.jp

<sup>2</sup>Department of Physics, Kyoto University, Kitashirakawa-oiwake-cho, Sakyo-ku, Kyoto 606-8502, Japan

<sup>3</sup>Department of Physics and Mathematics, Aoyama Gakuin University, Fuchinobe, Chuou-ku, Sagamihara 252-5258, Japan

<sup>4</sup>National Astronomical Observatory of Japan, Mitaka 181-8588, Japan

<sup>5</sup>Department of Astrophysics, Graduate School of Science, Osaka Prefecture University, 1-1 Gakuen-cho, Naka-ku, Sakai 599-8531, Japan

<sup>6</sup>Solar-Terrestrial Environment Laboratory, Nagoya University, Furo-cho, Chikusa-ku, Nagoya 464-8601, Japan

<sup>7</sup>LUPM, CNRS/Université Montpellier 2, France

Received \_\_\_\_\_; accepted \_\_\_\_\_

submitted version (26th January 2014)

## ABSTRACT

We have carried out a spectral analysis of the *Suzaku* X-ray data in the 0.4–12 keV range toward the shell-type very-high-energy  $\gamma$ -ray supernova remnant RX J1713.7–3946. The aims of this analysis are to estimate detailed X-rays spectral properties at a high angular resolution up to 2 arcmin, and to compare them with the interstellar matter. The X-ray spectrum is non-thermal and used to calculate absorbing column density, photon index, and absorption-corrected X-ray flux. The photon index varies significantly from 2.1 to 2.9. The hardest spectra are found in six positions at around 6–8 pc from the center, in two compact regions around dense molecular cloud cores as well as toward four extended diffuse regions with no molecular gas. We present an interpretation that diffusive shock acceleration with little turbulence realizes a high cut-off energy and the hardest spectra in the diffuse regions, where the shock speed is probably as high as  $\sim 6000$  km s $^{-1}$  and a gyro-factor is larger than 1. On the other hand, the turbulent fluid motion due to the shock-cloud interaction amplifies magnetic field around the dense cloud cores and decreases a gyro-factor close to the Bohme diffusion limit, leading to a high cut-off energy similar to the diffuse regions in spite of the shock deceleration. We suggest that the turbulent field may additionally accelerate the electrons in addition to the DSA in order to overcome the enhanced synchrotron loss due to the amplified field.

*Subject headings:* cosmic rays – ISM: clouds – ISM: individual objects (RX J1713.7–3946) – ISM: supernova remnants – X-rays: ISM

## 1. Introduction

Supernova remnants (SNRs) in the Galaxy are believed to be most likely accelerators of cosmic-rays (CRs) below “Knee”, in an energy range less than  $3 \times 10^{15}$  eV. The highest energy  $\gamma$ -rays in the Galaxy are emitted from three young and very-high-energy (VHE;  $E > 100$  GeV)  $\gamma$ -ray SNRs, RX J1713.7–3946 (Aharonian et al. 2004, 2006b, 2007), RX J0852.0–4622 (Aharonian et al. 2005, 2007), and HESS J1731–347 (H.E.S.S. Collaboration et al. 2011). In these SNRs, it is suggested that CR protons or electrons are accelerated efficiently up to 10–800 TeV or 1–40 TeV, respectively (e.g., Zirakashvili & Aharonian 2010). All the three show pure synchrotron X-rays with no thermal features, and acceleration of CR electrons is well established. The origin of the  $\gamma$ -rays in these SNRs, either hadronic or leptonic, has been under debate; the GeV  $\gamma$ -ray observations show hard  $\gamma$ -ray spectrum similar to that of the leptonic  $\gamma$ -rays (Abdo et al. 2011), whereas a recent comparative study between  $\gamma$ -rays and the interstellar protons is consistent with the hadronic origin of  $\gamma$ -rays (Fukui et al. 2012; Fukui 2013). It is notable that the numerical simulations on the shock-cloud interaction (Inoue et al. 2012) lend support for the hadronic  $\gamma$ -rays, since the low energy CR protons producing the GeV  $\gamma$ -rays cannot penetrate into the densest part of the cloud cores, leading to the hard spectrum just presented by Abdo et al. (2011).

Recent analyses showed that the spectral index of synchrotron X-rays (so called “photon index  $\Gamma$ ”) varies in the SNRs at resolutions of  $\sim 1$ –15 arcmin (e.g., Tanaka et al. 2008; Bamba et al. 2012; Kishishita et al. 2013). Since acceleration of CR electrons is established in RX J1713.7–3946, we are able to learn further details on the acceleration by a more thorough analysis of non-thermal X-rays. According to Inoue et al. (2012), the shock-cloud interaction amplifies the magnetic field around dense cloud cores and affects the electron spectrum significantly. The amplified field may intensify the non-thermal X-rays,

whereas the synchrotron loss due to the amplified field may decrease the number of CR electrons via synchrotron loss. In order to test such actions, we need a detailed comparison between the electron spectrum and the interstellar matter.

The young SNR RX J1713.7–3946 (also known as G347.3–0.5) is the best target for testing the action of the CR electrons, because the SNR emits strong synchrotron X-rays and VHE  $\gamma$ -rays (Pfeffermann & Aschenbach 1996; Enomoto et al. 2002; Aharonian et al. 2004, 2006a,b, 2007). RX J1713.7–3946 has a large apparent diameter of  $\sim 1$  degree at a small distance of  $\sim 1$  kpc (Fukui et al. 2003). Subsequently, the X-ray properties of RX J1713.7–3946 were studied by using *XMM-Newton*, *Suzaku*, and *Chandra*. Cassam-Chenaï et al. (2004) presented spatial distribution of absorbing column density  $N_{\text{H}}(\text{X-ray})$  and photon index  $\Gamma$  obtained by *XMM-Newton* at angular resolutions smoothed to 2–30 arcmin. The  $N_{\text{H}}(\text{X-ray})$  distribution shows significant variations over the whole SNR ( $0.4 \times 10^{22} \text{ cm}^{-2} \leq N_{\text{H}}(\text{X-ray}) \leq 1.1 \times 10^{22} \text{ cm}^{-2}$ ). The authors carried out an analysis of X-ray absorption and compared the X-rays with CO, HI, and visual extinction and showed that the interstellar medium (ISM) is correlated with the  $N_{\text{H}}(\text{X-ray})$ . Additionally, the value of photon index  $\Gamma$  has also shown the strong variation ( $1.8 \leq \Gamma \leq 2.6$ ). This trend was confirmed by a more detailed analysis of *XMM-Newton* data (Hiraga et al. 2005; Acero et al. 2009). *Chandra* observations revealed filamentary structures of X-rays and short time variability ( $\sim 1$  yr) of one of them (Uchiyama et al. 2003, 2007), which was interpreted as due to rapid particle acceleration of CR electrons and cooling in  $\sim 1$  yr scale. If this is correct, the cosmic-ray electrons should be accelerated efficiently in the “Bohm diffusion regime” (Uchiyama et al. 2007). Takahashi et al. (2008) and Tanaka et al. (2008) detected the hard synchrotron X-rays up to 40 keV from the SNR by using *Suzaku*. The spectra are fitted by interstellar absorbed power-law model with the exponential cut-off, suggesting CR electrons close to the Bohm diffusion limit (Tanaka et al. 2008).

Sano et al. (2010) presented multi-transition CO data and comparing with the *Suzaku* X-rays toward the northwest of RX J1713.7–3946. These authors found that the X-rays and molecular clumps are well-correlated at 1 pc scale, but anti-correlated at 0.1 pc scale. The latter shows a trend as rim-brightened X-rays around the dense molecular clumps. Subsequently, Sano et al. (2013) compared 18 CO clumps and a HI clump with their surrounding X-rays and concluded that the trend is commonly found over the whole SNR. Additionally, the authors found the strong correlation between the X-ray intensity and the molecular mass interacting with the SNR. These results indicate that the synchrotron X-rays are closely related to the surrounding CO gas. To explore this correlation, we should estimate the physical parameters such as the absorbing column density  $N_{\text{H}}(\text{X-ray})$ , photon index  $\Gamma$  and X-ray flux, in angular resolution high enough to compare with the ISM distributions. Such quantitative comparisons with the ISM mark an important step toward understanding the spectral variation of X-rays and efficient cosmic-ray acceleration.

In the present paper, we show a detailed comparison of the spatial distribution among  $N_{\text{H}}(\text{X-ray})$ ,  $\Gamma$ , X-ray flux and ISM both molecular and atomic gas at angular resolutions ranging from 2 arcmin to 8 arcmin depending on the photon statistics. Section 2 gives observations and data reduction of *Suzaku* X-rays, NANTEN CO and ATCA & Parkes HI. Section 3 consists of three subsections: Section 3.1 presents the typical spectra of X-rays; Section 3 spatial and spectral characterization of the X-rays; and 3.3 a detailed comparison with the ISM. Section 4 consists of three subsection: in Section 4.1 discusses the spatial variation of absorbing column density is discussed; Section 4.2 the relationship between X-ray flux and ISM; and Section 4.2.2 the efficient acceleration of cosmic-ray electrons. The conclusions are given in Section 5.

## 2. Observations and Data Reductions

### 2.1. X-rays

#### 2.1.1. Details of the datasets

We analyzed the X-ray dataset archive obtained by *Suzaku* (Data Archives and Transmission System; DARTS at ISAS/JAXA). This dataset consists of 17 pointings taken at 2005 September (SWG; 3 pointings), 2006 September and October (AO1; 10 pointings), 2010 February (AO4; 4 pointings) and we mainly used 15 pointing of ON sources (see also Figure 1). These data were already analyzed and published elsewhere (Takahashi et al. 2008; Tanaka et al. 2008; Sano et al. 2013) as summarized in Table 1 and Figure 1.

On board *Suzaku* are two active detectors, X-ray Imaging Spectrometer (XIS; Koyama et al. 2007) for imaging soft X-rays (0.2–12 keV) and Hard X-ray Detector (HXD; Takahashi et al. 2007) for hard X-rays (10–600 keV). In the present work, we deal with only the data taken with XIS. XIS consists of four CCDs located at the focus of X-ray Telescopes (XRTs; Serlemitsos et al. 2007); three of them are “Front-illuminated CCDs” (FI CCD; XIS 0, 2, and 3) and the other is “back-illuminated CCD” (BI CCD; XIS 1). Spaced-row charge injection technique (SCI; Nakajima et al. 2008; Uchiyama et al. 2009) was applied only to the four pointings in 2010 February. Unfortunately, XIS 2 was damaged by a micrometeorite hit on 2006 November 9 and the 2010 data in February consists of only XIS 0, 1, and 3. Subsequently, Segment A of XIS 0 was found to have anomaly on 2009 June 23 and Segment B was noticed to show charge leakage in part. We therefore used only the data from Segments C and D. We used Software HEASoft version 6.11 with pipeline processing version 2.0 or 2.4 and with standard event selection criteria (cleaned event files).

### 2.1.2. Imaging

The X-ray images are those used in Figure 2a of Sano et al. (2013). Figure 2 shows XIS mosaic image (1–5 keV) in RX J1713.7–3946 (Sano et al. 2013). Color scheme is in a square-root scale in  $10^{-4}$  counts  $\text{s}^{-1}$   $\text{pixel}^{-1}$  (pixel size is  $\sim 16.7''$ ) smoothed with a Gaussian kernel with FWHM  $\sim 45''$ . This image is subtracted for non X-ray background (NXB) and corrected for the vignetting effect by XRT (see more details in Sano et al. 2013 Section 2.3).

### 2.1.3. Spectroscopy

The X-ray spectra of RX J1713.7–3946 is represented by the absorbed power-law model (e.g., Koyama et al. 1997). This model is for synchrotron X-rays with photoelectric absorption and the model fitting gives three parameters, absorbing column density  $N_{\text{H}}(\text{X-ray})$ , and the photon index  $\Gamma$ , in addition to the absorption-corrected X-ray flux. We show typical X-ray spectra in Figure 3. We shall explain the method to derive the three parameters above. First, the SNR was divide into  $\sim 600$  regions of  $2' \times 2'$  grids, where the X-rays are significantly detected. For the  $\sim 600$  regions, only the data taken with FI CCD (XIS 0, 2, and 3) were used to derive X-ray spectra. In order to compare with the data of the interstellar medium, CO and HI, the angular resolution was set to the highest value (*Suzaku* HPD  $\sim 2'$ ). In addition, the background spectrum was estimated in the four regions shown in Figure 2 and the western background spectrum ( $\alpha_{\text{J2000}} = 17^{\text{h}}10^{\text{m}}31^{\text{s}}$ ,  $\delta_{\text{J2000}} = -39^{\circ}44'22.7''$ ) was used for every region. The two prominent point sources (1WGA J1714.4–3945 and 1WGA J1713.4–3949) in the field are excluded in the analysis. Subsequently, the spectra of each region taken with XIS 0, 2, and 3 are summed up and was fit by the absorbed power-law model to generate RMF (Redistribution Matrix File) by `xismfgen` and ARF (Ancillary Response File) by `xissimarfgen` (Ishisaki et al. 2007).

Next, in order to reduce the statistical relative errors in absorbing column density  $N_{\text{H}}(\text{X-ray})$  to less than 30%, some neighboring regions on source were summed up and the spectra were again fit by the absorbed power-law model. Figure 2 shows the final spectra with 305 regions as indicated by solid boxes. About one third of the whole SNR is 2' grid (4 arcmin<sup>2</sup>) and 80% of that is better than 4' grid (16 arcmin<sup>2</sup>). These values are much better than the previous studies (e.g., Cassam-Chenai et al. 2004, 70% of that is worse than 6' grid (36 arcmin<sup>2</sup>)). Each spectrum is binned to include at least 100 counts. After the binning the energy ranges a below 0.4 keV and above 12 keV bin are excluded in the fitting. The best fit parameters in the fitting were used to derive absorbing column density  $N_{\text{H}}(\text{X-ray})$ , photon index  $\Gamma$ , and absorption-corrected flux in 3–10 keV,  $F_{3-10\text{keV}}$ , as shown in Figure 4. If the background spectrum is changed to that for four to three regions, we see systematic errors of up to 10–20% in  $N_{\text{H}}(\text{X-ray})$ . This however does not significantly affect the results in Figure 4.

## 2.2. CO and HI

<sup>12</sup>CO( $J=1-0$ ) and HI datasets are NANTEN Galactic Plane Survey (NGPS) and Southern Galactic Plane Survey (SGPS) taken with NANTEN, and ATCA & Parkes telescopes (Moriguchi et al. 2005; McClure-Griffiths et al. 2005), respectively. The angular resolutions are HPBW  $\sim 2'.6$  for CO and  $\sim 2'.2$  for HI, similar to *Suzaku* XIS HPD  $\sim 2'$ . The velocity resolutions and typical rms noise fluctuations are (CO) 0.65 km s<sup>-1</sup> and 0.3 K ch<sup>-1</sup> and (HI) 0.82 km s<sup>-1</sup> and 1.9 K ch<sup>-1</sup>, respectively.

The velocity integrated intensities of CO and HI,  $W(\text{CO})$  and  $W(\text{HI})$ , are converted into molecular column density  $N(\text{H}_2)$  and atomic column density  $N_{\text{H}}(\text{HI})$  and the total proton column density is obtained as  $N_{\text{H}}(\text{H}_2+\text{HI}) = 2 \times N(\text{H}_2) + N_{\text{H}}(\text{HI})$ . A relationship  $N(\text{H}_2)$  (cm<sup>-2</sup>) =  $X_{\text{CO}}$  (cm<sup>-2</sup> (K km s<sup>-1</sup>)<sup>-1</sup>)  $\times W(\text{CO})$  (K km s<sup>-1</sup>) is used where  $X_{\text{CO}} = 2.0 \times 10^{20}$

( $\text{cm}^{-2} (\text{K km s}^{-1})^{-1}$ ) (Bertsch et al. 1993). The HI line is generally assumed to be optically thin and a relationship  $N_{\text{H}}(\text{HI}) = 1.823 \times 10^{18} \times W(\text{HI})$  is used (Dickey & Lockman 1990). The regions where the HI is optically we need to apply the correction for self-absorption. Details of the method is given by (Fukui et al. 2012) in Section 3.3.3.

### 3. Results

#### 3.1. Typical X-ray spectra

Figure 3 shows *Suzaku* XIS 0+2+3 spectra in the three typical regions, the north ( $\alpha_{\text{J2000}}, \delta_{\text{J2000}} = (17^{\text{h}}14^{\text{m}}19.95^{\text{s}}, -39^{\circ}28'31.11''$ ), the center ( $\alpha_{\text{J2000}}, \delta_{\text{J2000}} = (17^{\text{h}}13^{\text{m}}59.33^{\text{s}}, -39^{\circ}45'31.49''$ ), and the south ( $\alpha_{\text{J2000}}, \delta_{\text{J2000}} = (17^{\text{h}}12^{\text{m}}56.75^{\text{s}}, -40^{\circ}00'31.28''$ ), and the results of the model fitting. The lower parts show residuals in the fitting indicating that the fitting is reasonably good. We see no sign of thermal X-rays in Figure 3. The absorbing column density  $N_{\text{H}}(\text{X-ray})$  is  $\sim 0.5 \times 10^{22} \text{ cm}^{-2}$  both in the north and the center, but the photon index is different as  $\Gamma = 2.1 \pm 0.1$  and  $\Gamma = 2.7 \pm 0.1$  for the north and the center, respectively. On the other hand, the south has large absorbing column density  $N_{\text{H}}(\text{X-ray}) = 0.89_{-0.08}^{+0.09} \times 10^{22} \text{ cm}^{-2}$  and photon index  $\Gamma \sim 2.7$ . These differences are seen as significantly different spectral shapes in Figure 3. This confirms that the X-ray spectrum changes significantly from place to place as shown in the previous studies (e.g., Cassam-Chenaï et al. 2004; Tanaka et al. 2008)

### 3.2. Spatial and spectral characterization of the X-rays

#### 3.2.1. Absorbing column density

Figure 4a shows absorbing column density  $N_{\text{H}}(\text{X-ray})$  in the individual regions, where the *Suzaku* XIS 1–5 keV intensity is overlaid as contours. We aimed at achieving that the relative error is 30% at maximum at the 90% confidence level by tuning the pixel size. Consequently, the average relative error and its maximum value are confined to be 14% and 30%, respectively, at the 90% confidence level. This accuracy is high enough to assess the spatial variation of the absorbing column density and photon index as discussed later.

We find that the global distribution of  $N_{\text{H}}(\text{X-ray})$  shows a shell-like structure in Figure 4a. On the east side of center ( $\alpha_{\text{J2000}} \sim 17^{\text{h}}14.5^{\text{m}}$ ,  $\delta_{\text{J2000}} \sim -39^{\circ}40'$ ) and the west side of center ( $\alpha_{\text{J2000}} \sim 17^{\text{h}}13^{\text{m}}$ ,  $\delta_{\text{J2000}} \sim -39^{\circ}49'$ ),  $N_{\text{H}}(\text{X-ray})$  is as small as  $0.4\text{--}0.5 \times 10^{22} \text{ cm}^{-2}$  (region in blue). On the other hand, two regions in the northeast ( $\alpha_{\text{J2000}} \sim 17^{\text{h}}15^{\text{m}}$ ,  $\delta_{\text{J2000}} \sim -39^{\circ}25'$ ) and the northwest ( $\alpha_{\text{J2000}} \sim 17^{\text{h}}12^{\text{m}}$ ,  $\delta_{\text{J2000}} \sim -39^{\circ}30'$ ) show medium values of  $N_{\text{H}}(\text{X-ray}) = 0.7\text{--}1.0 \times 10^{22} \text{ cm}^{-2}$  (region in green), and part of the southwest ( $\alpha_{\text{J2000}} \sim 17^{\text{h}}12.5^{\text{m}}$ ,  $\delta_{\text{J2000}} \sim -40^{\circ}5'$ ) shows the largest  $N_{\text{H}}(\text{X-ray})$  with  $1.1\text{--}1.4 \times 10^{22} \text{ cm}^{-2}$  (region in red). Therefore, the absorbing column density varies from  $0.4 \times 10^{22} \text{ cm}^{-2}$  to  $1.4 \times 10^{22} \text{ cm}^{-2}$  within the SNR. These values are mostly consistent with the previous studies with *XMM-Newton* (Cassam-Chenaï et al. 2004, typical angular resolution  $\sim 8'$ ), while the angular resolution and the source coverage are better in the present study.

Figure 5 shows absorbing column density  $N_{\text{H}}(\text{X-ray})$  and visual extinction ( $A_{\text{V}}$  in unit of mag) derived from the Digitized Sky Survey I (DSS; Dobashi et al. 2005). The visual extinction is smoothed to the same binning with the X-rays. The values of  $A_{\text{V}}$  in Figure 5b are roughly classified into the three levels; low values ( $A_{\text{V}} < 2$  mag in blue) in the center of the SNR, medium values ( $2 \text{ mag} < A_{\text{V}} < 3$  mag in green) in the northeast and northwest

regions, and high values ( $A_V > 3$  mag in red) in the southwest. The general trend of  $A_V$  is similar to that of  $N_H(\text{X-ray})$ . Figure 6 shows a correlation plot between absorbing column density  $N_H(\text{X-ray})$  and visual extinction, showing a good correlation with a correlation coefficient of  $\sim 0.83$ .

### 3.2.2. Photon index and Flux

Figures 4b and 4c show the distributions of photon index  $\Gamma$  and absorption-corrected flux  $F_{3-10\text{keV}}$ , respectively. Their relative errors and maximum errors are  $\sim 6\%$  and  $13\%$  in Figure 4b, and  $\sim 7\%$  and  $23\%$  in Figure 4c at the 90% confidence level, respectively. Like absorbing column density, these quantities show significant spatial variation. In particular, photon index is largest with  $\Gamma \sim 3$  (in orange color) toward the center ( $\alpha_{\text{J2000}} \sim 17^{\text{h}}13.5^{\text{m}}$ ,  $\delta_{\text{J2000}} \sim -39^{\circ}48'$ ) and the central south ( $\alpha_{\text{J2000}} \sim 17^{\text{h}}13.5^{\text{m}}$ ,  $\delta_{\text{J2000}} \sim -40^{\circ}3'$ ). On the other hand, six regions with small photon index ( $\Gamma < 2.4$ ) are distributed as islands inside the SNR; the northwest ( $\alpha_{\text{J2000}} \sim 17^{\text{h}}11^{\text{m}}50^{\text{s}}$ ,  $\delta_{\text{J2000}} \sim -39^{\circ}32'30''$ ), the southwest ( $\alpha_{\text{J2000}} \sim 17^{\text{h}}12^{\text{m}}30^{\text{s}}$ ,  $\delta_{\text{J2000}} \sim -39^{\circ}56'30''$ ), the north ( $\alpha_{\text{J2000}} \sim 17^{\text{h}}14^{\text{m}}$ ,  $\delta_{\text{J2000}} \sim -39^{\circ}30'$ ), the east ( $\alpha_{\text{J2000}} \sim 17^{\text{h}}15^{\text{m}}$ ,  $\delta_{\text{J2000}} \sim -39^{\circ}40'$ ), and two regions in the southeast ( $\alpha_{\text{J2000}} \sim 17^{\text{h}}14^{\text{m}}30^{\text{s}}$ ,  $\delta_{\text{J2000}} \sim -39^{\circ}55'$ ) and ( $\alpha_{\text{J2000}} \sim 17^{\text{h}}15^{\text{m}}$ ,  $\delta_{\text{J2000}} \sim -40^{\circ}00'$ ). We do not discuss some regions with small photon index in the peripheral of the SNR where the statistics is worse than inside. The absorption-corrected flux  $F_{3-10\text{keV}}$  is similar to the 1–5 keV X-rays contours, especially at the brightest peaks in the northwest, west, and southwest. We also find another strong peak in the north ( $\alpha_{\text{J2000}} \sim 17^{\text{h}}13^{\text{m}}36^{\text{s}}$ ,  $\delta_{\text{J2000}} \sim -39^{\circ}37'31.7''$ ). These flux excesses are not due to a systematic error and are possibly connected with the ISM distribution as discussed in Section 3.3.

### 3.3. Comparison with the ISM: The X-ray flux, photon index and the ISM

Overlays of the interstellar gas at  $V_{\text{LSR}} = -20$  to  $2 \text{ km s}^{-1}$  with absorption-corrected flux  $F_{3-10\text{keV}}$  and photon index  $\Gamma$  are shown in Figure 7a and Figure 7b, respectively, where the ISM is total proton column density  $N_{\text{H}}(\text{H}_2+\text{HI})$  including derived from the CO and HI. The velocity range of the ISM associated is derived by Moriguchi et al. (2005) and is supported by Sano et al. (2013). based on a good correlation between the ISM and X-rays enhanced by the interaction with the SNR. We also annotated the positions (center of gravity) of the molecular clumps (crosses) and the HI clump (circle) defined by Sano et al. (2013). Additionally, we will hereinafter refer to the regions between the clumps as “inter-clump”. Figure 7a shows a trend that the X-rays are enhanced toward the regions with enhanced ISM in a pc scale. This trend is most significant in the west of the SNR, where the ISM is rich. On the other hand, in a sub-pc scale, we find that each bright spot of X-rays is lying around the CO and HI clumps except for the molecular clump in southwest ( $\alpha_{\text{J2000}} = 17^{\text{h}}12^{\text{m}}25.3^{\text{s}}$ ,  $\delta_{\text{J2000}} = -39^{\circ}55'7.4''$ ; named as “clump C”). These results are consistent with the previous study (Sano et al. 2013) and the present work has made it possible to evaluate the trend more quantitatively. Figure 8 shows a correlation plot between  $F_{3-10\text{keV}}$  and the ISM density; the linear correlation coefficients (hereafter LCC) are  $\sim 0.55$  (for the whole),  $\sim 0.19$  (the east, on the left side of  $\alpha_{\text{J2000}} \sim 17^{\text{h}}13^{\text{m}}38^{\text{s}}$ ) and  $\sim 0.54$  (west, on the right side of  $\alpha_{\text{J2000}} \sim 17^{\text{h}}13^{\text{m}}38^{\text{s}}$ ), respectively. The LCC  $\sim 0.55$  does not show strong correlation but the number of sample in the plot  $\sim 300$  indicates a positive correlation at a 5% confidence level according to a T-test (e.g., Taylor 1982).

In Figure 7b, we note that the regions having the hard spectrum are seen toward the enhanced ISM in the west, whereas the regions of the hard spectrum are also found toward the diffuse ISM in the east. Most outstanding are the ISM peaks toward/around the two X-ray peaks in the northwest ( $\alpha_{\text{J2000}} \sim 17^{\text{h}}11^{\text{m}}50^{\text{s}}$ ,  $\delta_{\text{J2000}} \sim -39^{\circ}32'30''$ ) and in the southwest

( $\alpha_{J2000} \sim 17^{\text{h}}12^{\text{m}}30^{\text{s}}$ ,  $\delta_{J2000} \sim -39^{\circ}56'30''$ ). In addition, we find four regions of the hard spectrum in the east where the ISM is diffuse ( $\alpha_{J2000} \sim 17^{\text{h}}15^{\text{m}}40^{\text{s}}$ ,  $\delta_{J2000} \sim -39^{\circ}58'00''$ ). Figure 9 shows a correlation plot showing that the relationship between the ISM and photon index is different between the west and east. In the west, the spectrum is hard when the ISM is dense and the spectrum is soft where the ISM is diffuse (LCC  $\sim -0.41$ ). In the east, the ISM is diffuse and the photon index shows variation (LCC  $\sim -0.08$ ), where the ISM density is not apparently related to the variation of the photon index for the whole region LCC is estimated to be  $\sim -0.16$ . Additionally, we show correlation plots between the photon index  $\Gamma$  and the absorption-corrected flux  $F_{3-10\text{keV}}$  in Figure 10. LCCs are  $\sim -0.62$  (the whole),  $\sim -0.53$  (the east) and  $\sim -0.81$  (the west), respectively. The histograms toward the west and east regions show a similar trend to the photon index distribution with respected the ISM density, while the west region has much higher X-ray fluxes than the east. We shall discuss about these results later in Section 4.2.2.

We summarize the main aspects of the present analysis as follows (Figures 7, 8, 9, and 10);

1. It is notable that the most intense X-rays are seen in the two region toward or around the CO peaks (Figure 7a). In the western half of the SNR, the ISM density is high with significant  $\text{H}_2$  and the X-rays are enhanced. In the eastern half of the SNR, the ISM density is low, being dominated by  $\text{H I}$ , and the X-rays are weak. The overall correlation between the ISM density and the X-rays is however not significantly high with a correlation coefficient of  $\sim 0.55$  (Figure 8).
2. The smallest X-ray photon index around 2.3 is seen toward the six regions; around/toward the two CO peaks in the west, and toward the four regions of low ISM density in the east (Figure 7b). The largest X-ray photon index around 3 is found toward the central region of the SNR as well as in the southern edge (Figure 7b).

3. The photon index shows a good correlation with the X-rays and the low photon index is seen toward regions of intense X-rays and vice versa (Figure 10). There is an offset by 0.3 in this correlation between the eastern and western halves of the SNR in the sense that the X-rays are more intense in the west, where the ISM is denser than in the east. The overall correlation between the photon index and the ISM density is not high (Figure 9).

## 4. Discussion

### 4.1. Spatial variation of the absorbing column density

The observations with *Suzaku* XIS have enabled us to estimate detailed distributions of the absorbing column density  $N_{\text{H}}(\text{X-ray})$  and photon index  $\Gamma$  in RX J1713.7–3946 at a low background level and high photon statistics. Here in the discussion, we first discuss the absorbing column density  $N_{\text{H}}(\text{X-ray})$ .

The spatial distribution of  $N_{\text{H}}(\text{X-ray})$  delineates the SNR shell as shown in Figure 5. This distribution shows a good correspondence with visual extinction. The regression in a straight line calculated from a least-squares fitting gives  $N_{\text{H}}(\text{X-ray}) \text{ (cm}^{-2}\text{)} = 3.0 \times 10^{21} \cdot A_{\text{V}}$  (magnitude) for the scatter plot in Figure 6. The numerical factor is slightly larger than that of the conventional relation  $N_{\text{H}} \text{ (cm}^{-2}\text{)} = 2.5 \times 10^{21} \cdot A_{\text{V}}$  (magnitude) (Jenkins & Savage 1974). This is understandable if we consider the distance of RX J1713.7–3946 is 1 kpc, since the visual extinction tends to be under-estimated for a distance larger than a few 100 pc by the foreground stars. It is not necessarily true that all  $N_{\text{H}}(\text{X-ray})$  is physically associated with the SNR. Here we need to take into account the contribution of the local gas between the SNR and the sun (Figure 11a). Moriguchi et al. (2005) already estimated the foreground component  $N_{\text{H,local}}(\text{H}_2+\text{HI})$  (Figure 11b). Figure 11c shows the distribution of

absorbing column density  $[N_{\text{H}}(\text{X-ray}) - N_{\text{H,local}}(\text{H}_2 + \text{HI})]$  in the SNR, which gives a shell-like distribution of  $N_{\text{H}}(\text{X-ray})$  more clearly than Figure 4a. The absorption toward the center of the SNR is  $\sim 0.2 \times 10^{22} \text{ cm}^{-2}$ , whereas that toward the outer boundary is shell-like with absorbing column density of  $\sim 0.5 - 0.8 \times 10^{22} \text{ cm}^{-2}$ . This shell represents a cavity wall of the ISM created by the stellar wind of the SNR progenitor. The inside of the cavity is highly evacuated with density lower than  $\sim 1 \text{ cm}^{-3}$  and the dense clumps in the cavity wall have higher density like  $\sim 10^2 - 10^4 \text{ cm}^{-3}$  (e.g., Sano et al. 2010; Inoue et al. 2012).

We shall discuss the absorption toward the southeast-rim. In this region Fukui et al. (2012) identified cold HI gas that corresponds to the VHE  $\gamma$ -ray shell. The cold HI with low spin temperature of  $\sim 40 \text{ K}$  has density around  $100 \text{ cm}^{-3}$ , less than  $\sim 1000 \text{ cm}^{-3}$  threshold density for the collisional excitation of the CO emission. The proton column density of the cold HI without CO emission is estimated to be  $\sim 0.5 \times 10^{22} \text{ cm}^{-2}$  from the HI self-absorption in the southeast rim of RX J1713.7–3946 (Fukui et al. 2012). The present absorption in the SNR calculated from X-rays has also column density of  $0.4 - 0.5 \times 10^{22} \text{ cm}^{-2}$  (Figure 11c) which is consistent with the cold HI.

We compared the absorbing column density  $[N_{\text{H}}(\text{X-ray}) - N_{\text{H,local}}(\text{H}_2 + \text{HI})]$  (Figure 11c) with  $N_{\text{H}}(\text{H}_2 + \text{HI})$ , the proton column density physically associated with the X-ray emitting shell, in two velocity ranges of the interacting gas in Figures 12 and 13. Figures 12a and 12b show  $[N_{\text{H}}(\text{X-ray}) - N_{\text{H,local}}(\text{H}_2 + \text{HI})]$  overlaid on the ISM proton column density  $N_{\text{H}}(\text{H}_2 + \text{HI})$  at  $V_{\text{LSR}} \sim -20$  to  $-9 \text{ km s}^{-1}$  and  $\sim -9$  to  $2 \text{ km s}^{-1}$ . This comparison shows that the ISM distribution has generally good correspondence with the X-ray absorbing column density. It is however to be noted that the blue-shifted ISM shows a poorer correlation than that of the red-shifted ISM with the X-ray absorbing column density as shown in Figure 13, scatter plots between the ISM and the X-ray absorption column density. In Figure 13 we divide the plots into the red- and blue-shifted ISM. The blue-shifted ISM in

the west shows a poor correlation with the X-ray absorbing column density of  $LCC \sim 0.25$ , while the red-shifted ISM in the west has a higher correlation of  $LCC \sim 0.39$  than the blue-shifted ISM. This indicates that the red-shifted ISM is located on the far-side of the SNR, and it is in the opposite sense to what is expected in an expanding motion of the shell-like ISM. The relative position of the ISM is explicable if the pre-existent cloud motion is dominant for the dense CO gas instead of expansion, as already suggested to explain the velocity distribution of the HI self-absorption Fukui et al. (2012).

## 4.2. Relationship between the X-ray flux, the photon index, and the X-ray absorption/the ISM

### 4.2.1. Shock-cloud interaction

Inoue et al. (2012) showed by magnetohydrodynamic (MHD) numerical simulations that the X-ray intensity is closely correlated with the ISM by the enhanced magnetic field around dense clumps due to turbulence in the shock-cloud interaction. The interaction creates correlation between the ISM and X-rays at a pc scale via the magnetic field. Observations by Sano et al. (2010, 2013) showed that pc-scale correlation is seen between the X-ray intensity and the clump mass interacting with the SNR blast waves, as well as anti-correlation between them in a sub-pc scale due to exclusion of the CR electrons in the dense clumps. The distributions of the X-ray intensity in Figure 7a at grid sizes of 2–8 arcmin (0.6–2.4 pc) show their interrelation at a pc scale; we see trend that the X-rays are enhanced in the west where the ISM is rich, and that the X-rays are depressed in the east where the ISM is poor. This is consistent with what is expected in the shock-cloud interaction scheme. The higher dispersion in Figure 8 may be in part ascribed to anti-correlation at a sub-pc scale, consistent with the suggestion by Sano et al. (2010, 2013).

#### 4.2.2. Efficient cosmic-ray acceleration

Based on the present results on the photon index (Figure 4b), we discuss the efficient cosmic-ray acceleration in RX J1713.7–3946. As shown by the previous works (Takahashi et al. 2008; Tanaka et al. 2008), the photon index in the 1–10keV range reflects cutoff-energy  $\varepsilon_0$  of the synchrotron X-rays. The small (large) photon index corresponds to large (small) cutoff energy. According to the standard DSA scheme, the cut-off energy of synchrotron photons  $\varepsilon_0$  is given as follows when the synchrotron cooling is effective (Zirakashvili & Aharonian 2007),

$$\varepsilon_0 = 0.55 \times (v_{\text{sh}} / 3000 \text{ km s}^{-1})^2 \eta^{-1} \text{ (keV)}, \quad (1)$$

where  $v_{\text{sh}}$  is the shock speed and  $\eta = \delta B^2 / B^2$  ( $>1$ ) a gyro-factor, the degree of magnetic field fluctuations. In particular the limit of  $\eta = 1$  is called as Bohme diffusion limit corresponding to highly turbulent conditions and, accordingly, the cutoff-energy is likely determined by the shock speed and turbulence.

The present results suggest that in the west of the SNR, where the ISM is rich, the shock-cloud interaction is effective and turbulence is enhanced around dense ISM clumps. On the other hand, in the east of the SNR where the ISM is poor the DSA alone is mainly working without shock-cloud interaction. We show a schematic image summarizing the relevant features in Figure 14. The shaded regions in blue, white, and orange correspond to the photon index  $\Gamma < 2.4$  (small) ,  $2.4 < \Gamma < 2.8$  (medium), and  $\Gamma > 2.8$  (large), respectively. Sano et al. (2013) presented that the innermost cavity of 3–4 pc radius is surrounded by the ISM shell consisting of the dense clumps and the inter-clump gas. The inter-clump gas is shown by the shaded gray region around the clumps in Figure 14. The dense clumps have density of  $10^2$  to  $10^4 \text{ cm}^{-3}$  (Sano et al. 2010, 2013) and are mainly distributed in the west toward the Galactic plane. The inter-clump gas has density  $< 2 \text{ cm}^{-3}$ , as given by the upper limit from no thermal X-rays (Takahashi et al. 2008), and we

shall adopt density of the inter-clump gas to be  $1 \text{ cm}^{-3}$  for discussion. We assume that density in the cavity is  $\sim 0.25 \text{ cm}^{-3}$ , the same with that estimated toward Gum nebula where the gas is swept up by the strong stellar winds from  $\zeta$  Pup (Wallerstein & Silk 1971; Gorenstein et al. 1974). In this scheme, DSA is efficiently taking place in the cavity and the accelerated CRs are injected into the ISM shell. Figure 14 show that the shock waves are now interacting with the five dense clumps and has passed through two clumps denoted as “C” and “L” (see for the nomenclature Sano et al. 2013).

Table 2 gives two sets of possible parameters for discussion in the two cases with different ISM density, although they are crude at best (c.f., Tanaka et al. 2008). In the west where the shock-cloud interaction is working, the magnetic field may be amplified up to  $\sim 1$  mG as indicated by the short time variation of  $\sim 1$  yr in the synchrotron X-rays by *Chandra*, where the Bohme diffusion limit ( $\eta = 1$ ) is a good approximation (Uchiyama et al. 2007). On the other hand, the shock speed  $v_{\text{sh}}$  is proportional to  $1/\sqrt{n}$  and is decreased in the dense ISM, where  $n$  is the average number density of the ISM. The observational result shows that  $v_{\text{sh}}$  is decreased to  $4500 \text{ km s}^{-1}$  or less, and we shall assume  $\sim 3000 \text{ km s}^{-1}$  (Uchiyama et al. 2007; Zirakashvili & Aharonian 2007). It is probable that in the west of the SNR, mainly the shock-cloud interaction causes large cutoff-energy and a small photon index. On the other hand, in the east the shock speed is not much decelerated in the lower density. A possible scenario is as follows; the average ISM density in the east is about 1/4 of that in the west and the shock speed  $v_{\text{sh}}$  becomes larger by a factor of 2. Then,  $\eta$  becomes larger than 1, but the term (the shock speed  $v_{\text{sh}}$ )<sup>2</sup> is more effective. If we assume the shock speed is  $\sim 6000 \text{ km s}^{-1}$  and  $\eta \sim 4$ , the cutoff-energy becomes larger as  $\sim 0.6$  keV (Tanaka et al. 2008) and the photon index smaller. The trend in the photon index, therefore, is largely explicable by the DSA scheme with modification due to the ISM gas.

The regions where the photon index is small in the east seem to be located toward the

edge of medium density clumps along the outer part of the shell (Figure 7b). It is however not likely that this small photon index is due to the shock-cloud interaction, because the spatial extent with  $\Gamma < 2.4$  is four times larger than that in the west. It is predicted that the area where the cutoff-energy (photon index) is above (below) a certain value becomes small with the increase of the magnetic field if the Sedov-Taylor evolution is assumed (equation (9) in Kishishita et al. 2013). This implies that the field is stronger in the east than in the west, but it is inconsistent with the shock-cloud interaction. It is therefore reasonable that the acceleration is mainly by DSA in the east not by the shock-cloud interaction.

In Figure 14, the innermost part of the SNR having the large photon index  $\Gamma > 2.8$  is shown by orange color. We suggest that the electrons there have lower cut-off energy due to synchrotron cooling over the last 1000 yrs; for magnetic field of  $10 \mu\text{G}$  the CR electron cooling time at 10 keV is small as  $\sim 500$  yrs, whereas that at 1 keV is large as  $\sim 1500$  yrs, leading to low cut-off energy in the central 3–4 pc.

One would expect that the photon index becomes even larger toward the denser regions, if only  $v_{\text{sh}}$  determines the photon index. Interestingly, the photon index becomes small toward the clump C and the region between the two dense clumps, D and L in Figure 7b. It is also notable that the X-rays are enhanced toward these regions having small photon indexes. In the shock-cloud interaction scheme, the magnetic field is amplified in the interacting region, leading to higher synchrotron loss and smaller cut-off energy. This can lead to lower X-ray intensity and lower cut-off energy toward the dense clumps, while obviously we need a more elaborate work to quantitatively affirm this. It is thus possible that the observed trend may not be explained by only a DSA scheme. We here suggest that some additional acceleration mechanism is working to accelerate CR particles in the west where the ISM is rich. Such mechanisms include the 2nd order Fermi acceleration (Fermi 1949) and/or magnetic reconnection in the turbulent medium (Hoshino 2012). In the

latter case, compression in the shocked region creates multiple magnetic islands and causes magnetic reconnection that leads to outflow and accelerate high-energy particles emitting enhanced synchrotron radiation. This scenario is consistent with the shock-cloud interaction picture presented for RX J1713.7–3946 (Inoue et al. 2012) and multiple magnetic islands may be formed around the dense ISM clumps.

To summarize, we suggest that the ISM and its distribution have a significant impact on the scheme of the particle acceleration via the shock-cloud interaction. This suggests the tight relationship between the SNR and the ISM. The present study explored the CR electron behavior into significant details not achieved in the previous works, and presented that the ISM density affects significantly the CR electron cut-off energy. In particular, dense molecular clumps excites turbulent in the shock waves, amplifying the magnetic field. The CR electron cut-off energy is increased in spite of such amplified field, and we suggest that additional electron acceleration may be taking place in such turbulent regimes around the dense clumps.

In near future, Cherenkov Telescope Array (CTA) will provide information on the spectral distribution of  $\gamma$ -rays over the SNR at 1 arcmin resolution and will allow us to investigate the spectra and acceleration of both the CR protons and electrons. In addition, the soft X-ray spectrometer (SXS) of ASTRO-H will probe yet undetected thermal X-rays by sensitive high-energy resolution spectroscopy in RX J1713.7–3946. We can then probe the fraction of the energy of the SNR blast waves used for cosmic-ray acceleration. And the hard X-ray imager (HXI) of ASTRO-H will resolve photon index distribution at 10 keV or higher, possibly allowing us to constrain electron energy spectrum models by comparing that below 10 keV (e.g., Yamazaki et al. 2013). These future instruments will enable more accurate measurements of the efficient cosmic-ray acceleration.

## 5. Conclusions

We summarize the present work as follows.

1. We have estimated the spatial distribution of absorbing column density, photon index, and absorption-corrected flux (3–10 keV) comparable to the scale of the ISM distribution, a few arcmin, by using *Suzaku* archival data with low background.
2. The X-ray flux shows enhancement toward the dense ISM. This is consistent with the shock-cloud interaction model by (Inoue et al. 2012) that X-rays become bright around the dense cloud cores due to turbulence amplification of magnetic field.
3. Photon index shows a large variation within the SNR from  $\Gamma = 2.1$ – $2.9$ . The photon index shows smallest values around the dense regions of cloud cores as well as toward diffuse regions with no molecular gas. This trend can be described as a cut-off energy variation of CR electrons (Zirakashvili & Aharonian 2007). We present possible parameters to explain the variation of the cut-off energy under the DSA scheme. The enhanced intensity and harder spectra of the X-rays toward the dense clumps may require additional electron acceleration toward the dense clumps possibly via magnetic reconnection or other mechanism incorporating magnetic turbulence.
4. The absorbing column density shows a good correlation with the visual extinction. We found that the southeast-rim identified by HI self-absorption, which shows enhanced VHE  $\gamma$ -rays has a clear counterpart in the X-ray absorption too, lending new support to the HI self-absorption interpretation.

NANTEN2 is an international collaboration of 10 universities; Nagoya University, Osaka Prefecture University, University of Cologne, University of Bonn, Seoul National

University, University of Chile, University of New South Wales, Macquarie University, University of Sydney, and University of ETH Zurich. This work was financially supported by a grant-in-aid for Scientific Research (KAKENHI, No. 24-10082, No. 21253003, No. 23403001, No. 22540250, No. 22244014, No. 23740149, No. 23740154 (T.I.), No. 22740119, and No. 24224005) from the Ministry of Education, Culture, Sports, Science and Technology of Japan (MEXT). This work was also financially supported by the Young Research Overseas Visits Program for Vitalizing Brain Circulation (R2211) and the Institutional Program for Young Researcher Overseas Visits (R29) by Japan Society for the Promotion of Science (JSPS) and by the Mitsubishi Foundation and by the grant-in-aid for Nagoya University Global COE Program, “Quest for Fundamental Principles in the Universe: From Particles to the Solar System and the Cosmos”, from MEXT. This research made use of data obtained from Data ARchives and Transmission System (DARTS), provided by Center for Science-satellite Operation, and Data Archive (C-SODA) at ISAS/JAXA.

## REFERENCES

- Abdo, A. A., Ackermann, M., Ajello, M., et al. 2011, *ApJ*, 734, 28
- Acero, F., Ballet, J., Decourchelle, A., et al. 2009, *A&A*, 505, 157
- Aharonian, F. A., Akhperjanian, A. G., Aye, K.-M., et al. 2004, *Nature*, 432, 75
- Aharonian, F., Akhperjanian, A. G., Bazer-Bachi, A. R., et al. 2005, *A&A*, 437, L7
- Aharonian, F., Akhperjanian, A. G., Bazer-Bachi, A. R., et al. 2006, *ApJ*, 636, 777
- Aharonian, F., Akhperjanian, A. G., Bazer-Bachi, A. R., et al. 2006, *A&A*, 449, 223
- Aharonian, F., Akhperjanian, A. G., Bazer-Bachi, A. R., et al. 2007, *A&A*, 464, 235
- Aharonian, F., Akhperjanian, A. G., Bazer-Bachi, A. R., et al. 2007, *ApJ*, 661, 236
- Bamba, A., Pühlhofer, G., Acero, F., et al. 2012, *ApJ*, 756, 149
- Bertsch, D. L., Dame, T. M., Fichtel, C. E., et al. 1993, *ApJ*, 416, 587
- Berezhko, E. G., & Völk, H. J. 2006, *A&A*, 451, 981
- Berezhko, E. G., & Völk, H. J. 2008, *A&A*, 492, 695
- Berezhko, E. G., & Völk, H. J. 2010, *A&A*, 511, A34
- Butt, Y. M., Torres, D. F., Combi, J. A., Dame, T., & Romero, G. E. 2001, *ApJ*, 562, L167
- Cassam-Chenai, G., Decourchelle, A., Ballet, J., et al. 2004, *A&A*, 427, 199
- Dickey, J. M., & Lockman, F. J. 1990, *ARA&A*, 28, 215
- Dobashi, K., Uehara, H., Kandori, R., et al. 2005, *PASJ*, 57, 1
- Ellison, D. C., & Vladimirov, A. 2008, *ApJ*, 673, L47

- Ellison, D. C., Patnaude, D. J., Slane, P., & Raymond, J. 2010, *ApJ*, 712, 287
- Ellison, D. C., Slane, P., Patnaude, D. J., & Bykov, A. M. 2012, *ApJ*, 744, 39
- Enomoto, R., Tanimori, T., Naito, T., et al. 2002, *Nature*, 416, 823
- Fang, J., Zhang, L., Zhang, J. F., Tang, Y. Y., & Yu, H. 2009, *MNRAS*, 392, 925
- Fermi, E. 1949, *Physical Review*, 75, 1169
- Fukui, Y., Moriguchi, Y., Tamura, K., et al. 2003, *PASJ*, 55, L61
- Fukui, Y., Sano, H., Sato, J., et al. 2012, *ApJ*, 746, 82
- Fukui, Y. 2013, in *Astrophysics and Space Science Proc. 34, 2nd Session of the Sant Cugat Forum on Astrophysics*, ed. Diego F. Torres & O. Reimer (Berlin: Springer), 249
- Gorenstein, P., Harnden, F. R., Jr., & Tucker, W. H. 1974, *ApJ*, 192, 661
- Hiraga, J. S., Uchiyama, Y., Takahashi, T., & Aharonian, F. A. 2005, *A&A*, 431, 953
- Huang, C.-Y., Park, S.-E., Pohl, M., & Daniels, C. D. 2007, *Astroparticle Physics*, 27, 429
- Hoshino, M. 2012, *Physical Review Letters*, 108, 135003
- H.E.S.S. Collaboration, Abramowski, A., Acero, F., et al. 2011, *A&A*, 531, A81
- Inoue, T., Yamazaki, R., & Inutsuka, S.-i. 2009, *ApJ*, 695, 825
- Inoue, T., Yamazaki, R., Inutsuka, S.-i., & Fukui, Y. 2012, *ApJ*, 744, 71
- Ishisaki, Y., Maeda, Y., Fujimoto, R., et al. 2007, *PASJ*, 59, 113
- Jenkins, E. B., & Savage, B. D. 1974, *ApJ*, 187, 243
- Taylor J. R. 1982 *An introduction to error analysis* (2nd ed.; California: USB)

- Kishishita, T., Hiraga, J., & Uchiyama, Y. 2013, *A&A*, 551, A132
- Koyama, K., Kinugasa, K., Matsuzaki, K., et al. 1997, *PASJ*, 49, L7
- Koyama, K., Tsunemi, H., Dotani, T., et al. 2007, *PASJ*, 59, 23
- Li, H., Liu, S., & Chen, Y. 2011, *ApJ*, 742, L10
- Malkov, M. A., Diamond, P. H., & Sagdeev, R. Z. 2005, *ApJ*, 624, L37
- Maxted, N. I., Rowell, G. P., Dawson, B. R., et al. 2012, *MNRAS*, 422, 2230
- McClure-Griffiths, N. M., Dickey, J. M., Gaensler, B. M., Green, A. J., Haverkorn, M., & Strasser, S. 2005, *ApJS*, 158, 178.
- Moriguchi, Y., Tamura, K., Tawara, Y., et al. 2005, *ApJ*, 631, 947
- Moraitis, K., & Mastichiadis, A. 2007, *A&A*, 462, 173
- Morlino, G., Amato, E., & Blasi, P. 2009, *MNRAS*, 392, 240
- Muraishi, H., Tanimori, T., Yanagita, S., et al. 2000, *A&A*, 354, L57
- Nakajima, H., Yamaguchi, H., Matsumoto, H., et al. 2008, *PASJ*, 60, 1
- Pannuti, T. G., Allen, G. E., Houck, J. C., & Sturmer, S. J. 2003, *ApJ*, 593, 377
- Pfeffermann, E., & Aschenbach, B. 1996, in *Roentgenstrahlung from the Universe*, MPE Report 263, ed. H. U. Zimmermann, J. H. Trümper, & H. Yorke, 267
- Reimer, O., & Pohl, M. 2002, *A&A*, 390, L43
- Sano, H., Sato, J., Horachi, H., et al. 2010, *ApJ*, 724, 59
- Sano, H., Tanaka, T., Torii, K., et al. 2013, *ApJ*, 778, 59

- Serlemitsos, P. J., Soong, Y., Chan, K.-W., et al. 2007, PASJ, 59, 9
- Slane, P., Gaensler, B. M., Dame, T. M., et al. 1999, ApJ, 525, 357
- Takahashi, T., Abe, K., Endo, M., et al. 2007, PASJ, 59, 35
- Takahashi, T., Tanaka, T., Uchiyama, Y., et al. 2008, PASJ, 60, 131
- Tanaka, T., Uchiyama, Y., Aharonian, F. A., et al. 2008, ApJ, 685, 988
- Uchiyama, Y., Aharonian, F. A., & Takahashi, T. 2003, A&A, 400, 567
- Uchiyama, Y., Aharonian, F. A., Takahashi, T., et al. 2005, High Energy Gamma-Ray Astronomy, 745, 305
- Uchiyama, Y., Aharonian, F. A., Tanaka, T., Takahashi, T., & Maeda, Y. 2007, Nature, 449, 576
- Uchiyama, H., Ozawa, M., Matsumoto, H., et al. 2009, PASJ, 61, 9
- Wallerstein, G., & Silk, J. 1971, ApJ, 170, 289
- Wang, Z. R., Qu, Q.-Y., & Chen, Y. 1997, A&A, 318, L59
- Weaver, R., McCray, R., Castor, J., Shapiro, P., & Moore, R. 1977, ApJ, 218, 377
- Yamazaki, R., Ohira, Y., Sawada, M., & Bamba, A. 2013, arXiv:1301.7499
- Yuan, Q., Liu, S., Fan, Z., Bi, X., & Fryer, C. L. 2011, ApJ, 735, 120
- Zhang, L., & Yang, C. Y. 2011, PASJ, 63, 89
- Zirakashvili, V. N., & Aharonian, F. 2007, A&A, 465, 695
- Zirakashvili, V. N., & Aharonian, F. A. 2010, ApJ, 708, 965

Table 1. SUMMARY OF THE *Suzaku* ARCHIVE DATA OF RX J1713.7–3946

Pointing ID	ObsID	$\alpha_{J2000}$ ( <sup>h</sup> <sup>m</sup> <sup>s</sup> )	$\delta_{J2000}$ ( <sup>°</sup> <sup>'</sup> <sup>''</sup> )	XIS Exp. (ks)	Date	SCI
0.....	100026010	17 12 17.0	–39 56 11	69	2005 Sep 26	OFF
1.....	501063010	17 11 51.5	–39 31 13	18	2006 Sep 11	OFF
2.....	501064010	17 12 38.0	–39 40 14	21	2006 Sep 11	OFF
3.....	501065010	17 12 38.2	–39 22 15	22	2006 Sep 11	OFF
4.....	501066010	17 11 04.5	–39 40 10	21	2006 Sep 12	OFF
5.....	501067010	17 11 05.1	–39 22 10	21	2006 Sep 12	OFF
6.....	501068010	17 14 11.6	–39 40 14	21	2006 Sep 13	OFF
7.....	501069010	17 14 11.4	–39 22 15	18	2006 Sep 19	OFF
8.....	501070010	17 14 11.8	–39 58 14	21	2006 Sep 19	OFF
9.....	501071010	17 12 17.6	–39 18 50	21	2006 Sep 20	OFF
10.....	501072010	17 15 44.5	–39 40 10	20	2006 Oct 5	OFF
11.....	504027010	17 11 50.8	–39 31 00	62	2010 Feb 15	ON
12.....	504028010	17 13 14.0	–40 14 22	19	2010 Feb 16	ON
13.....	504029010	17 12 39.8	–40 01 50	21	2010 Feb 17	ON
14.....	504030010	17 15 39.0	–40 00 47	22	2010 Feb 17	ON
OFF1.....	100026020	17 09 31.9	–38 49 24	35	2005 Sep 25	OFF
OFF2.....	100026030	17 09 05.1	–41 02 07	38	2005 Sep 28	OFF

Note. — The details of datasets are also shown in Takahashi et al. (2008), Tanaka et al. (2008), and Sano et al. (2013).

Table 2. AN EXAMPLE OF THE PHYSICAL PARAMETERS FOR THE CUT-OFF ENERGY

Region	Gas density $n$ ( $\text{cm}^{-3}$ )	Gyro-factor $\eta$	Shock speed $v_{\text{sh}}$ ( $\text{km s}^{-1}$ )	Cut-off energy $\varepsilon_0$ (keV)
Inter-clump	$1^\dagger$	$1^\ddagger$	$3000^\ddagger$	$0.6^\S$
Inside of the cavity	$0.25^*$	4	6000	0.6

Note. —  $^\dagger$ Inoue et al. (2012); Sano et al. (2013),  $^*$ Wallerstein & Silk (1971); Gorenstein et al. (1974),  $^\ddagger$ Uchiyama et al. (2007); Zirakashvili & Aharonian (2007),  $^\S$ Takahashi et al. (2008); Tanaka et al. (2008)

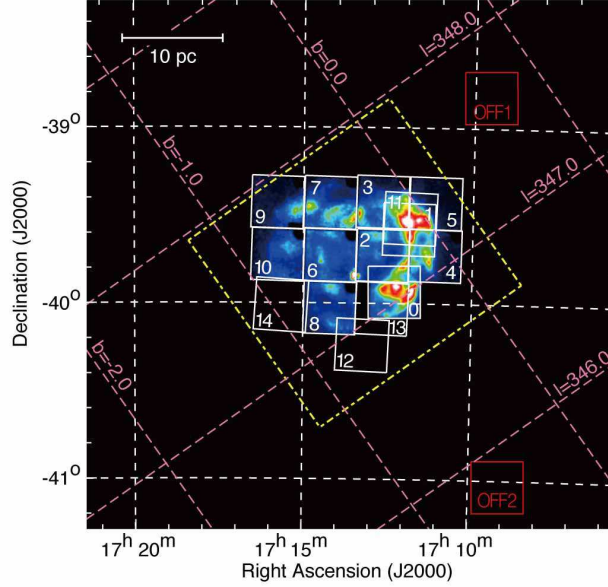


Fig. 1.— *Suzaku* field of view (FoV) of each observation area toward the SNR RX J1713.7–3946 overlaid on the *Suzaku* XIS mosaic image (1–5 keV) taken from Tanaka et al. (2008). The small squares correspond to the FoV of the *Suzaku* XIS. The numbers indicated in the *Suzaku* XIS FoV are pointing IDs according to Tanaka et al. (2008); Sano et al. (2013) and used throughout this paper (see also Table 1). The large polygon (enclosed by the yellow dash-dot line) corresponds to observed areas in the  $^{12}\text{CO}(J=1-0)$  emission taken with the NANTEN telescope. We also show the galactic coordinates in the magenta dashed lines.

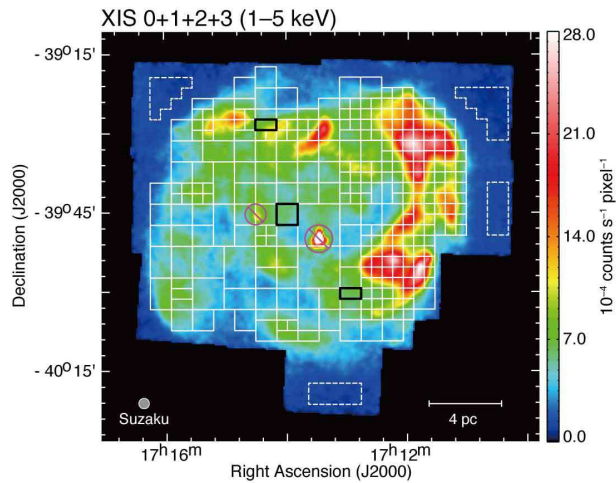


Fig. 2.— *Suzaku* XIS mosaic image of RX J1713.7–3946 in the energy band 1–5 keV (Sano et al. 2013). The color scale indicates count rate on a square root scale and is unit of  $10^{-4}$  counts  $s^{-1}$  pixel $^{-1}$ . The solid boxes are those used for spectral analysis. We also show the spectra enclosed by the black solid lines (see also Figure 3). The dashed boxes correspond to the regions used to extract the background spectrum. The two point sources, 1WGA J1714.4–3945 and 1WGA J1713.4–3949, are circled with magenta and those regions were ignored from spectral analysis.

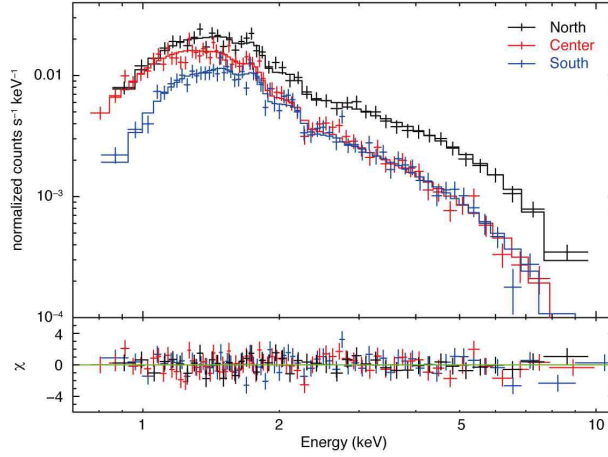


Fig. 3.— Typical X-ray spectra of north (black), center (red) and south (blue) regions (for the regions definition see Figure 2). The solid lines represent in the best-fit absorbed power-law model. The lower part shows the residuals from the best-fit models. The north and center spectra are the same absorbing column density ( $N_{\text{H}}(\text{X-ray}) \sim 0.5 \times 10^{22} \text{ cm}^{-2}$ ) but with different photon index (north:  $\Gamma = 2.1 \pm 0.1$ , center:  $\Gamma = 2.7 \pm 0.1$ ). The center and south spectra are the same photon index ( $\Gamma \sim 2.7$ ) but with different absorbing column densities (center:  $N_{\text{H}}(\text{X-ray}) = 0.45^{+0.06}_{-0.05} \times 10^{22} \text{ cm}^{-2}$ , south:  $N_{\text{H}}(\text{X-ray}) = 0.89^{+0.09}_{-0.08} \times 10^{22} \text{ cm}^{-2}$ ).

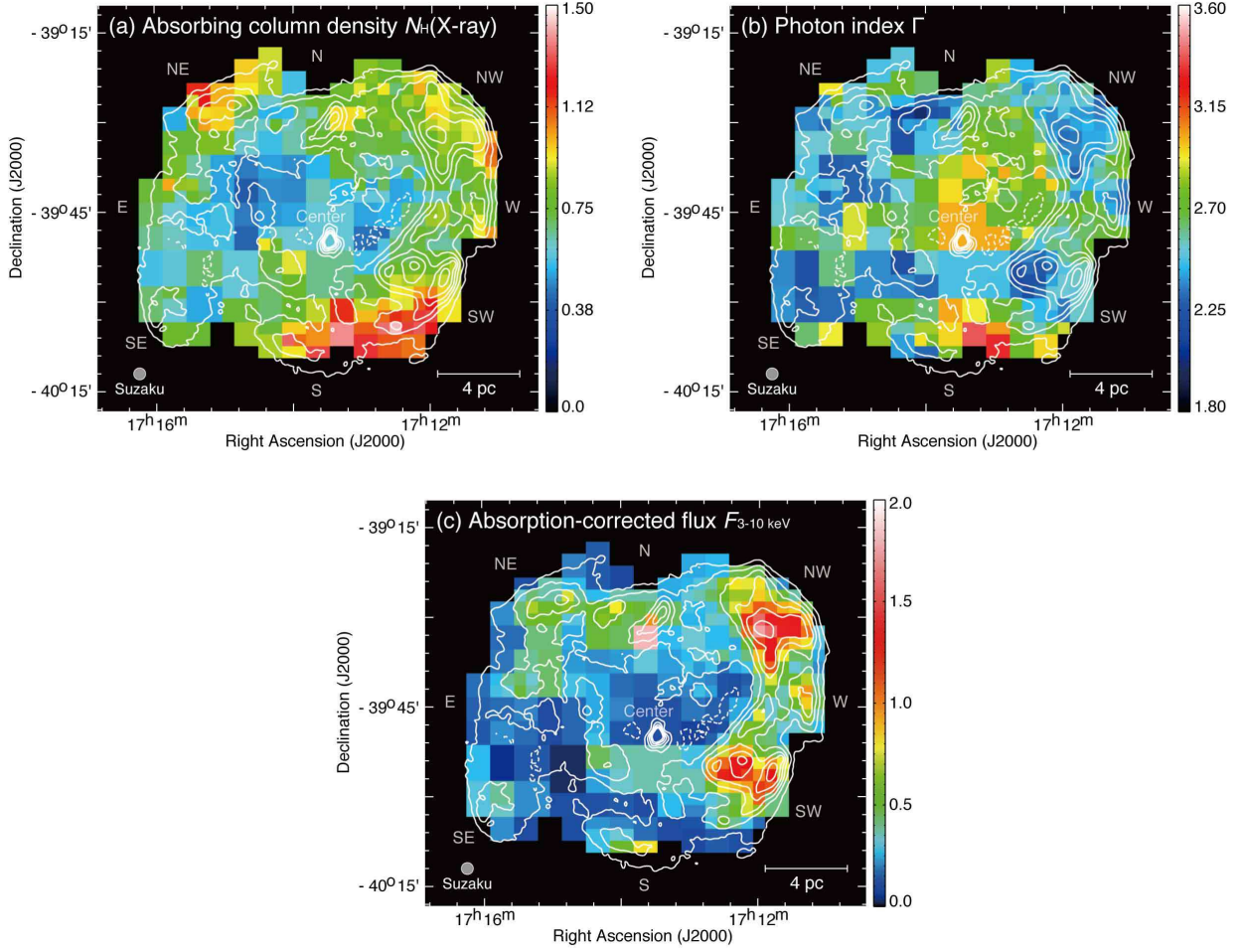


Fig. 4.— Maps of the best-fit parameters, (a) absorbing column density  $N_{\text{H}}(\text{X-ray})$ , (b) photon index  $\Gamma$ , and (c) absorption-corrected X-ray flux  $F_{3-10\text{keV}}$ , for absorbed power-law model. All maps overlaid with smoothed contours of the *Suzaku* XIS mosaic images. The contour levels are from at  $3.9 \times 10^{-4}$  counts  $\text{s}^{-1}$  pixel $^{-1}$  and are square root spaced up to  $23.9 \times 10^{-4}$  counts  $\text{s}^{-1}$  pixel $^{-1}$  with a pixel size of  $\sim 16''7$ . The color schemes in (a–b) and (c) are liner and square root scale, respectively. The units are  $10^{22}$   $\text{cm}^{-2}$  for  $N_{\text{H}}(\text{X-ray})$  and  $10^{-12}$   $\text{erg cm}^{-2} \text{s}^{-1}$  for  $F_{3-10\text{keV}}$ .

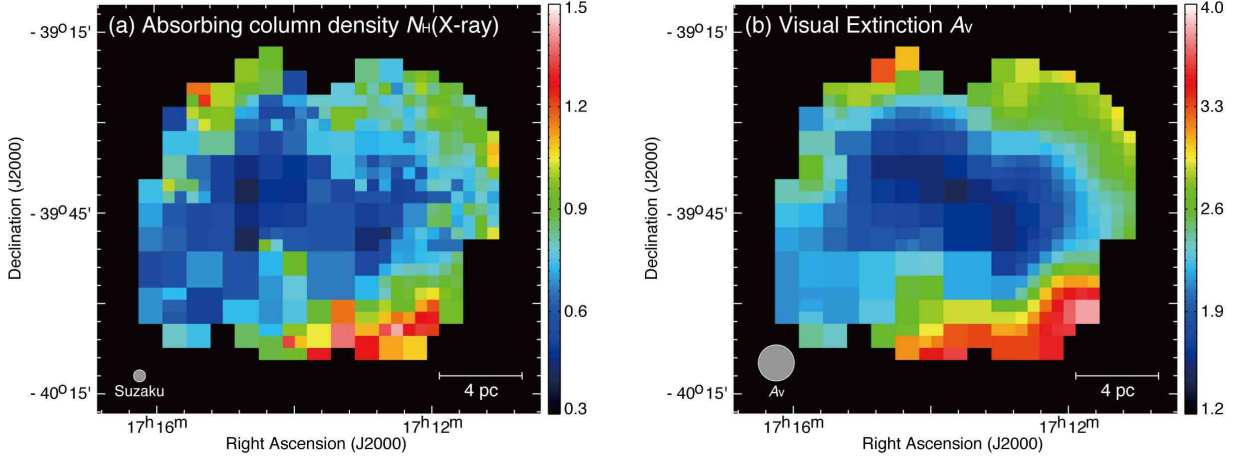


Fig. 5.— (a) Distribution of the absorbing column density  $N_{\text{H}}(\text{X-ray})$  as Figure 4 (b), but the color scale is changed. (b) Distribution of the visual extinction  $A_{\text{v}}$  (Dobashi et al. 2005). The grid separations are the same as (a).

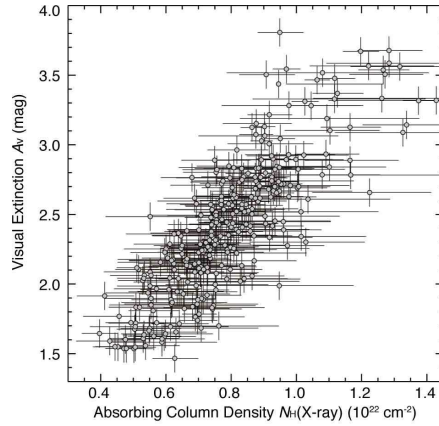


Fig. 6.— Correlation plot between the absorbing column density  $N_{\text{H}}(\text{X-ray})$  (in units of  $10^{22} \text{ cm}^{-2}$ ) and the visual extinction  $A_{\text{v}}$  (in units of mag). The error bars are given at a 90% confidence level in  $N_{\text{H}}(\text{X-ray})$ .

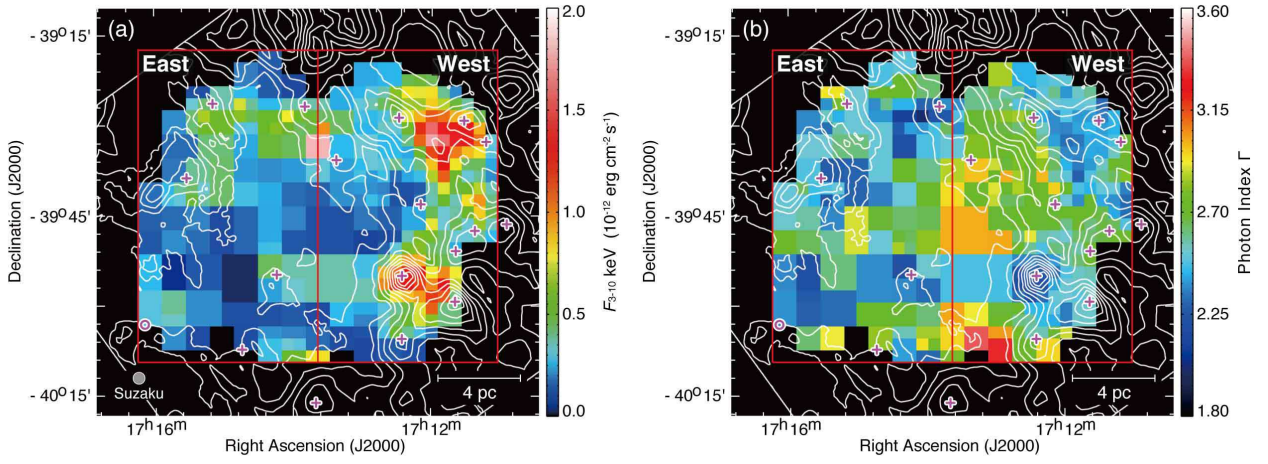


Fig. 7.— Distribution of (a) the absorption-corrected flux  $F_{3-10\text{keV}}$  and (b) photon index  $\Gamma$  as Figure 4. The contours indicate the proton column density  $N_{\text{H}}(\text{H}_2+\text{HI})$  in a velocity range from  $-20$  to  $2 \text{ km s}^{-1}$ . The contour levels are  $0.6, 0.75, 0.90, 1.1, 1.3, 1.5, 1.7, 1.9,$  and  $2.1 \times 10^{22} \text{ cm}^{-2}$ . The magenta crosses and circle are corresponded to the positions of CO and HI clumps (Sano et al. 2013).

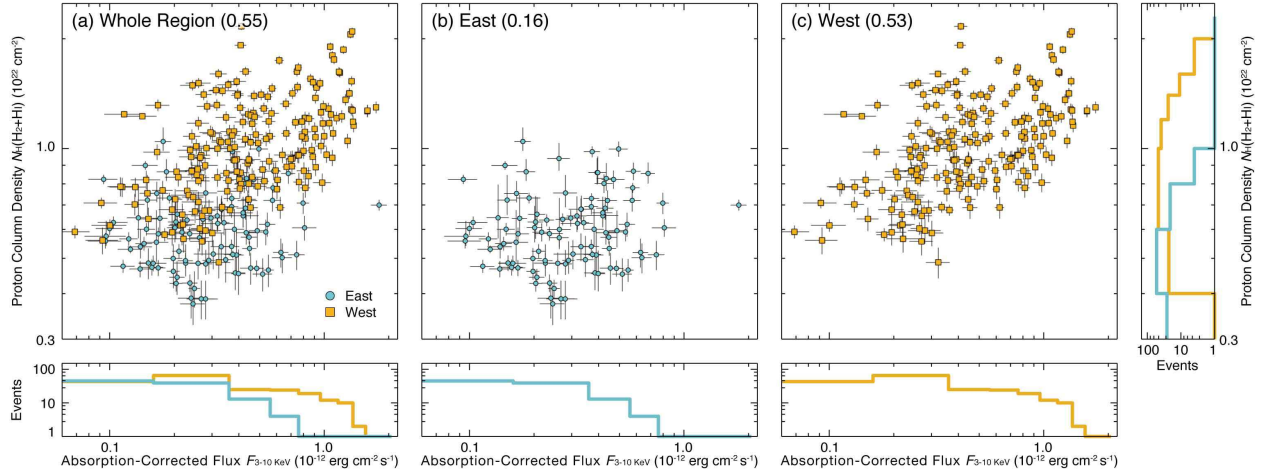


Fig. 8.— Correlation plot between the absorption-corrected flux  $F_{3-10\text{keV}}$  and the proton column density  $N_{\text{H}}(\text{H}_2+\text{HI})$  in (a) whole region, (b) East and (c) West. The regions are defined as follow Figure 7:  $\circ$  for East,  $\square$  for West. The histograms are also shown at lower or right side of each plot. All plots, the scale is square-root.

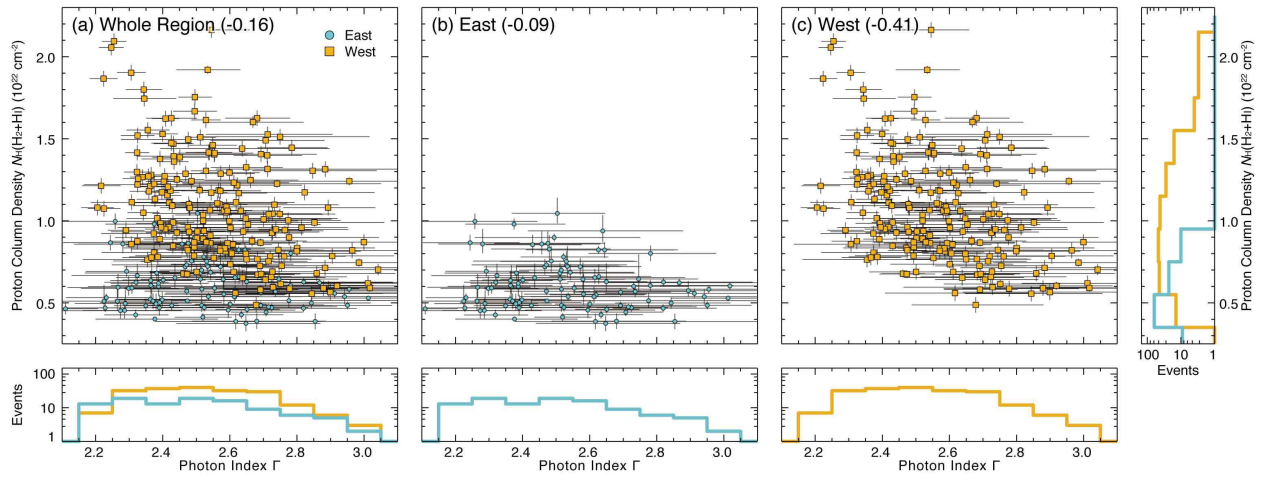


Fig. 9.— Correlation plot between the photon index  $\Gamma$  and the proton column density  $N_{\text{H}}(\text{H}_2+\text{HI})$  in (a) whole region, (b) East, and (c) West. All plots, the scale is linear.

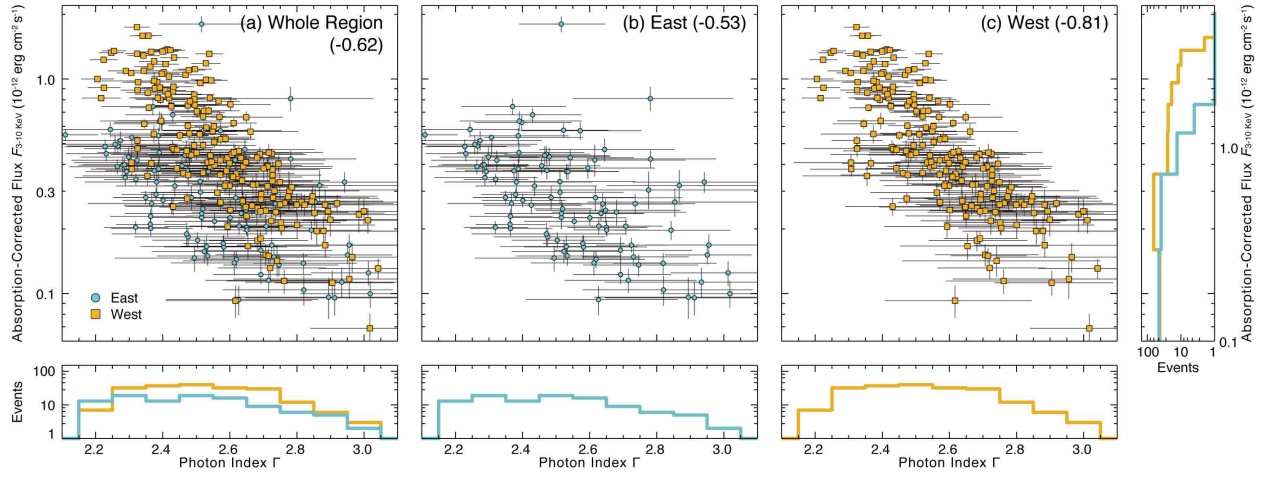


Fig. 10.— Correlation plot between the photon index  $\Gamma$  and the absorption-corrected flux  $F_{3-10\text{keV}}$  in (a) whole region, (b) East, and (c) West. The scale is linear in the photon index  $\Gamma$  and is square-root in the absorption-corrected flux  $F_{3-10\text{keV}}$ .

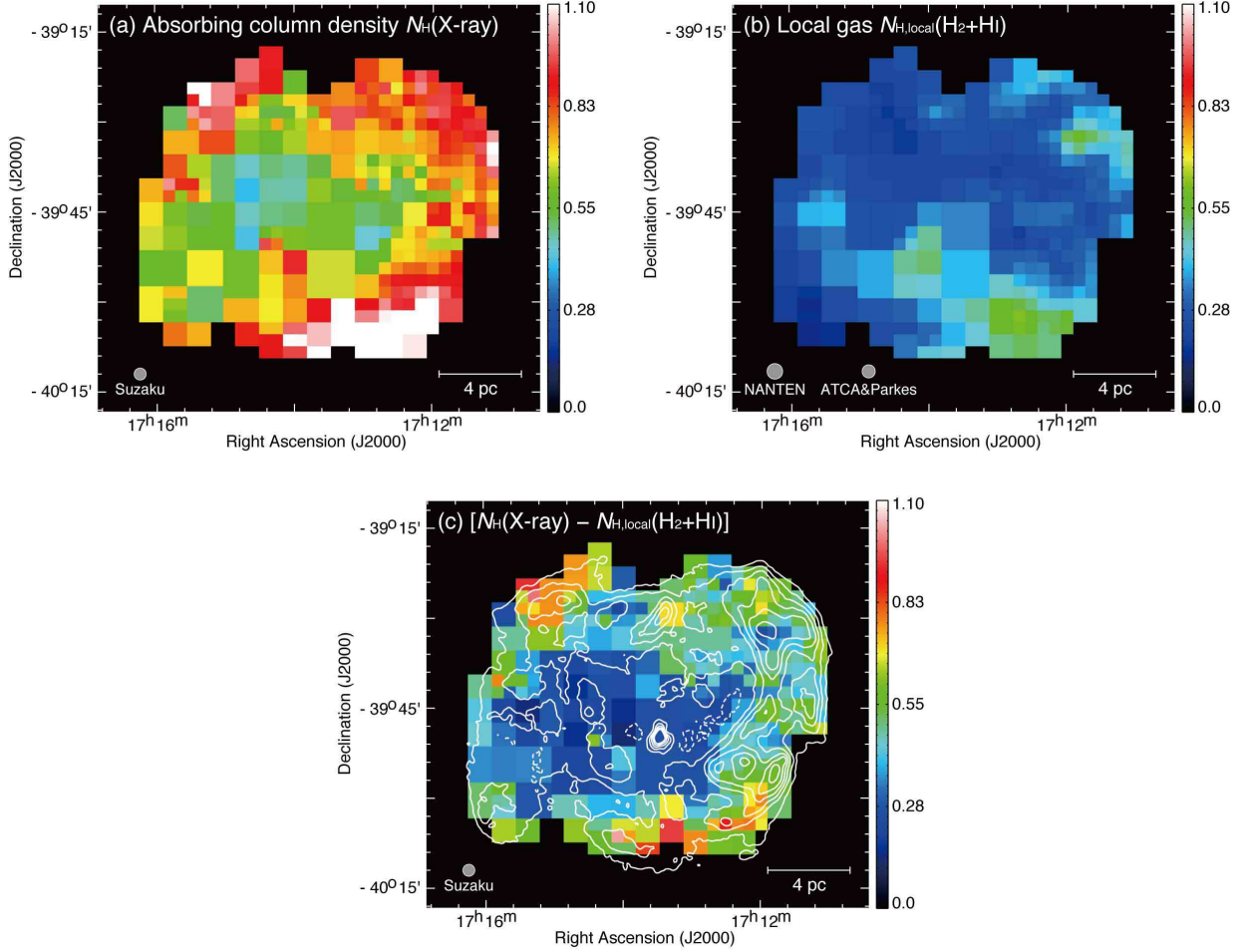


Fig. 11.— (a) Distribution of the absorbing column density  $N_{\text{H}}(\text{X-ray})$  as Figure 4 (a), but the color scale is changed to stress the region of the low absorbing column density. (b) Distribution of the proton column density in local gas  $N_{\text{H,local}}(\text{H}_2+\text{HI})$  estimated by using the CO and HI data sets. (c) Distribution of the absorbing column density  $[N_{\text{H}}(\text{X-ray}) - N_{\text{H,local}}(\text{H}_2+\text{HI})]$  overlaid with smoothed contours of the *Suzaku* XIS mosaic images as shown in Figure 4. All images are the same color scale.

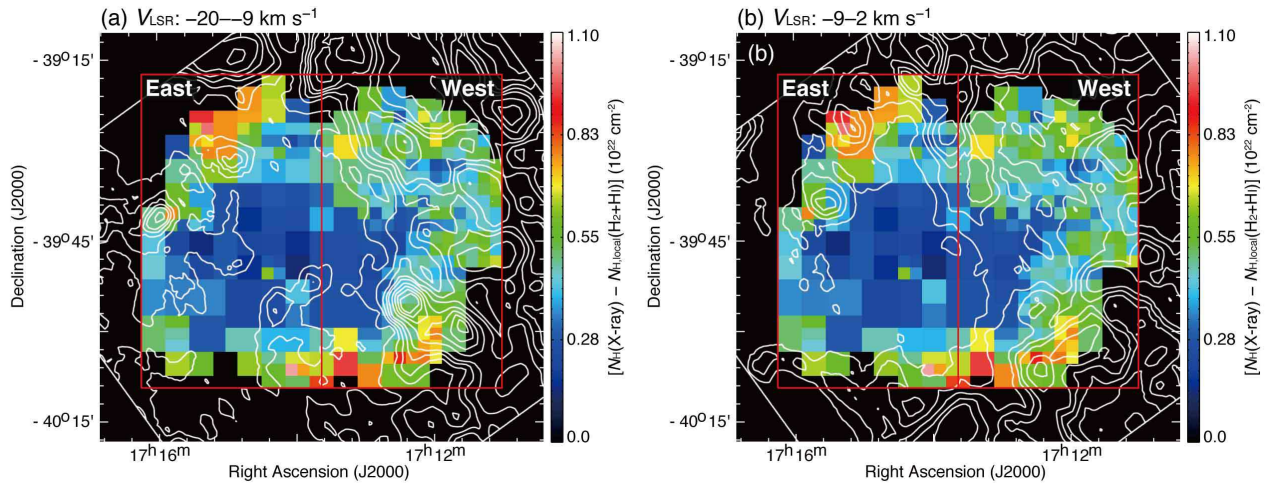


Fig. 12.— Distribution of the absorbing column density  $[N_{\text{H}}(\text{X-ray}) - N_{\text{H,local}}(\text{H}_2 + \text{HI})]$  as Figure 7 (c) superposed on the proton column density  $N_{\text{H}}(\text{H}_2 + \text{HI})$  in the velocity range from (a)  $-20$  to  $-9 \text{ km s}^{-1}$  and from (b)  $-9$  to  $2 \text{ km s}^{-1}$ , respectively. The contour levels are  $0.4, 0.5, 0.6, 0.7, 0.9, 1.1, 1.3,$  and  $1.5 \times 10^{22} \text{ cm}^{-2}$ . The regions, East and West, where used for the correlation plots (see Figure 13).

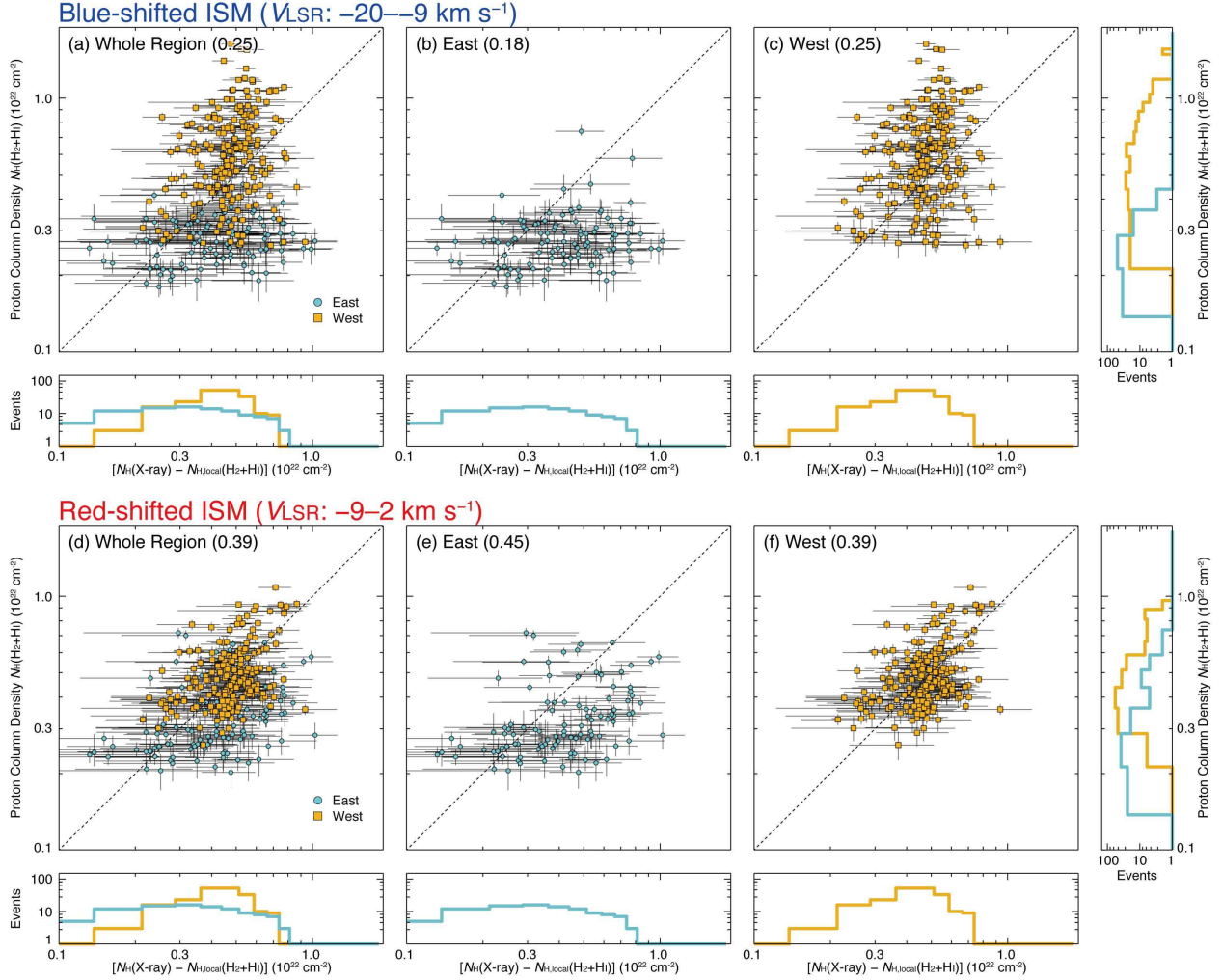


Fig. 13.— Correlation plot between the absorbing column density  $[N_{\text{H}}(\text{X-ray}) - N_{\text{H,local}}(\text{H}_2 + \text{HI})]$  and the proton column density  $N_{\text{H}}(\text{H}_2 + \text{HI})$  in the velocity range from (a–c)  $-20$  to  $-9 \text{ km s}^{-1}$  and from (d–f)  $-9$  to  $2 \text{ km s}^{-1}$ , respectively. The regions indicate (a, d) whole region, (b, e) East, and (c, f) West, respectively. The dashed lines are the bisector for each panel. The histograms are also shown at lower or right side of each plot. All plots, the scale is square-root.

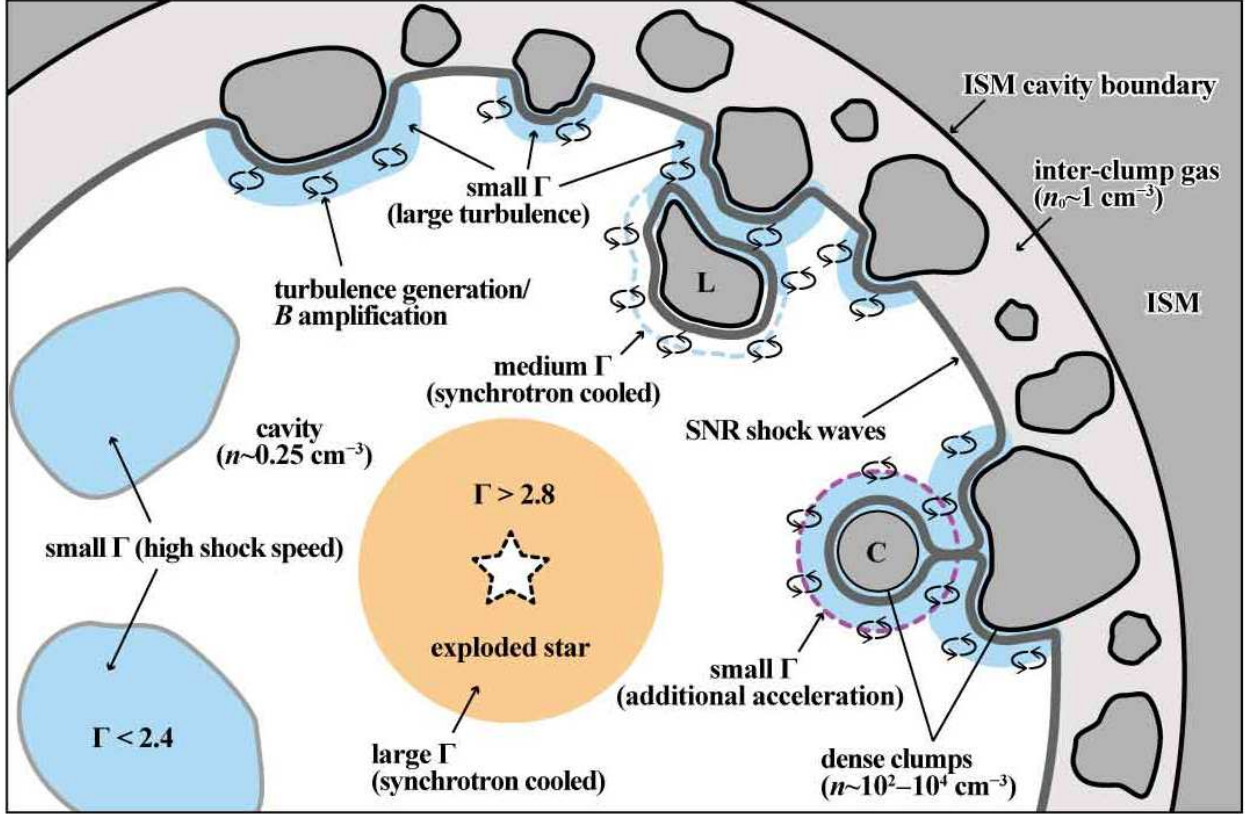


Fig. 14.— Schematic image of the efficient cosmic-ray acceleration toward RX J1713.7–3946. The SNR shock waves travel through the cavity (gas density  $n \sim 0.25 \text{ cm}^{-3}$ ), where cosmic-ray acceleration is working by DSA scheme and the shock speed is not much decelerated in lower density. Propagated shock waves are stalled toward the dense clumps, and is traveling in the inter-clump space. Shock-cloud interaction generates the turbulence ( $\eta \sim 1$ ) and enhances the magnetic field around the dense clumps. The accelerated particles in the innermost cavity and some of clumps are already cooled down due to the synchrotron cooling. The additional acceleration is induced due to the high turbulence and strong magnetic fields around the some of dense clumps (see for more details the text).